HAL
open science

# Effect of vibrations on granular material flows down an inclined plane using DEM simulations

Naïma Gaudel, Sébastien Kiesgen de Richter

## To cite this version:

Naïma Gaudel, Sébastien Kiesgen de Richter. Effect of vibrations on granular material flows down an inclined plane using DEM simulations. Powder Technology, 2019, 346, pp.256-264. 10.1016/j.powtec.2019.01.080 . hal-02090172

**HAL Id: hal-02090172**

**https://hal.univ-lorraine.fr/hal-02090172v1**

Submitted on 22 Oct 2021

**HAL** is a multi-disciplinary open access archive for the deposit and dissemination of scientific research documents, whether they are published or not. The documents may come from teaching and research institutions in France or abroad, or from public or private research centers.

L'archive ouverte pluridisciplinaire **HAL**, est destinée au dépôt et à la diffusion de documents scientifiques de niveau recherche, publiés ou non, émanant des établissements d'enseignement et de recherche français ou étrangers, des laboratoires publics ou privés.

Distributed under a Creative Commons Attribution - NonCommercial 4.0 International License

Version of Record: https://www.sciencedirect.com/science/article/pii/S0032591019300828
Manuscript_d78a005fe42d2d41754ac320cb2ddabf

# Effect of vibrations on granular material flows down an inclined plane using DEM simulations

Naïma Gaudel[1,*], Sébastien Kiesgen De Richter[1]

*Laboratoire d'Énergétique et de Mécanique Théorique et Appliquée (LEMTA), Université de Lorraine - CNRS, UMR 7563, Vandœuvre-lès-Nancy 54505, France*

**Abstract**

The influence of transverse mechanical vibrations on dense flows of granular material down inclines with a rough bed is analyzed using 3D DEM simulations and compared with experimental results. The vibrations make appear two distinct behaviors: a gravity-driven regime and a vibration-driven regime. In the gravity-driven regime, our results are consistent with previous studies from the literature. The vibrations induce particles velocity fluctuations in the vibration-driven regime, which generate a granular temperature profile along the depth of the packing related to the velocity profile. The velocity profile is consistent with a creeping flow which makes appear a critical length scale related to a nonlocal rheology. Our results suggest that this length scale emerges from the characteristic damping length of transverse vibration waves which propagate in the bulk of the granular material. These results could be of interest for the optimization of powders conveying.

*Keywords:* Granular material, Vibrations, DEM simulations, Rheology, Inclined plane, Powders conveying

*Corresponding author
*Email address:* naima.gaudel@univ-lorraine.fr (Naïma Gaudel)



© 2019 published by Elsevier. This manuscript is made available under the CC BY NC user license
https://creativecommons.org/licenses/by-nc/4.0/

## 1. Introduction

Industries are looking for tests, correlations, or even rheological models to predict the flow of granular matter during transport, in relation with some measurable physical features. It is also of prime importance that correlations and models take into account the impact of vibrations (amplitude, frequency) on the rheological behavior and the structure (rupture, granulation) of granular flows. Optimizing their transport requires a better understanding of the influence of a large number of parameters (size and morphology of particles, viscosity of the interstitial fluid, volume fraction, intensity of the applied vibrations, geometrical and confinement effects, ...) on the rheological properties of vibrated granular matter. From a fundamental point of view, studying the influence of vibrations on the flowing behavior of granular dispersions represents a fascinating interplay between the jamming transition in dense granular dispersions and rheology.

The flow of granular dispersions in the absence of vibrations has extensively been studied in the literature, both experimentally [1, 2, 3, 4, 5, 6, 7] and numerically [8, 9, 10, 11, 12, 13, 14, 15]. In these papers, it has been shown that a visco-plastic $\mu(I)$ rheology describes very well the flow of such dispersions. The dynamical friction coefficient $\mu$, and therefore the yield stress, depends on the dimensionless number $I$ which is the ratio of the internal reorganization time of the dispersion to the typical timescale of the flow. When vibrations are applied, the behavior of granular dispersions is drastically altered. In particular, previous studies have shown that the rheology is modified by changing local blockages properties at the grain scale [16, 17, 18, 19, 20, 21] and therefore the conditions for flow arrest. For instance, the constitutive law for vibrated granular flows down inclines should have a friction coefficient which depends on the shear rate, the dispersion properties, and the vibration intensity through the relative acceleration $\Gamma = \left(A(2\pi f)^2\right)/g$; with $A$ and $f$ the amplitude and

the frequency of the vibrations, respectively. In particular, vibrations modify the deposits by permitting grains reorganizations close to the flow arrest (see Gaudel *et al.* [22]).

In this paper, we numerically study how vibrations influence the limit between the jammed and the unjammed regime as well as the apparent rheology $\mu(I)$. The Fig. 1 is a hypothetical phase-diagram of what is expected when vibrations are added to a gravitational flow of a granular dispersion tilted from an angle $\theta$. The addition of vibrations make possible flows below the critical angle $\theta_c$, defined as the angle below which no flow can occur without vibrations. The higher the tilt angle, the smaller the value of $\Gamma$ required to trigger the flow. Contrary to experiments, with DEM simulations we can easily extract the flow profiles in the bulk of the granular material for a wide range of parameters (vibration intensity, inclination angle, particle properties). In this paper, we exhibit (i) how vibrations make appear possible flows below the angle of avalanche, (ii) how vibrations control the deposits, the critical angle and thus the apparent rheology of granular material, and (iii) how vibration induced flows are related to a characteristic length scale which depends on the relative acceleration $\Gamma$. The results are compared with the ones previously obtained experimentally (see Ref. [22]).

## 2. Simulation methods

### *2.1. Presentation of the model*

In this work, 3D discrete element simulations (DEM) are performed. This model is based on the method developed by Cundall and Strack [23]. It consists in a Lagrangian tracking of each particle. The particle-particle and particle-wall contacts are modeled using the soft-sphere approach, i.e. the overlapping is allowed to compute the forces. The particle motion is assessed in a deterministic

way, i.e. by solving the Newtonian equations of motion. The DEM scheme used in this study is based on the open-source software LIGGGHTS (**L**AMMPS for **I**mproved **G**eneral **G**ranular and **G**ranular **H**eat **T**ransfer **S**imulations) [24, 25].

The aim of this paper is to simulate monodisperse glass beads ($\rho = 2500\,\mathrm{kg/m^3}$, $d = 6$ mm) flows down a rough and vibrated plane ($\rho = 2500$ kg/m$^3$, $\lambda = 18$ and 30 mm). In the framework of such flows [8, 11, 26, 27, 28], the particle properties chosen for our DEM simulations are the following: Coulomb friction $\mu = 0.5$, Young modulus $E = 5 \times 10^6$ N/m$^2$, Poisson ratio $\nu = 0.45$, restitution coefficient $e = 0.6$, coefficient of friction particle/particle and particle/wall $\mu_{pp} = \mu_{pw} = 0.5$, and coefficient of rolling friction particle/particle and particle/wall $\mu_{rpp} = \mu_{rpw} = 0.02$. The integration time step is chosen to be (i) a multiple of the period of the vibrations $T = 1/f$ and (ii) much smaller than $T$. The order of magnitude is $\delta t \sim 10^{-6}$ s $\ll T$. Data are saved every $X$ time step, such as $X \times \delta t = T/4$. Physical quantities presented in this paper are then averaged over the period of the vibrations.

The specific feature of this work is the addition of vibrations in the simulations. For that, the $xy$- plane is caused to move by oscillations. The oscillations are initiated by choosing a period. This period depends on the chosen frequency $f$, and an amplitude $A$ according to the $y$- direction (see Fig. 2). The amplitude range studied in this paper is $A = [0.001 \text{ to } 6.40]\, d$ [1].

A detailed description of the Hertz-Mindlin model [29, 30] used in this work can be found in the Appendix A.

### *2.2. Geometry and particle properties*

A typical snapshot from simulation is presented in Fig. 2. The studied system is made of $N$ monodisperse spherical particles (defined as the system size in this paper) of diameter $d$ and mass $m$ flowing down an inclined chute geometry. The simulations volume consists of a rectangular box with a chute

base area$^2$ equals $20d \times 100d$, a rough bed in the $xy$- plane, an open top, and periodic conditions in both $x$ and $y$ directions. This simulation cell is tilted by an angle $\theta$ with respect to the direction of gravity $g$. The flow is induced in the $x-$direction, and can reach a steady state thanks to a rough bottom. This rough bed is created by fixing a thin layer of particles, with the same properties as the bulk ones and a diameter $\lambda$. The relative roughness of the studied system is defined as $d/\lambda$. These particles are distributed over the base of the system with a volume fraction similar to 45% (see dark particles in Fig. 2). The steady state is defined as proposed in some previous studies [13, 14], i.e. by checking (i) the stationarity of the surface velocity in time and (ii) the uniformity of the velocity profile. Since the simulations employ periodic boundary conditions in the $y-$direction, they are not influenced by side walls effects that are known to change the profiles significantly [7, 15]. Therefore, the simulations are similar to measurements obtained in the central part of a real chute flow. A summary of the simulations that have been performed can be found in the Appendix B.

## 3. Results and discussions

### *3.1. Phase diagram*

The phase behavior of granular particles in chute flow is determined by the height of the flow $h$ and the tilt angle $\theta$, as proposed in 2D by Pouliquen and Renault [31]. This study exhibits the existence of a flow line, defined as the boundary between flow and no-flow regions. This flow line is characterized by Pouliquen [1] and later verified by Daerr and Douady [32]. Using empirical argument, Pouliquen suggested the following analytic relation:

$$\tan\theta = \tan\theta_1 + (\tan\theta_2 - \tan\theta_1)\exp\left(-\frac{h_{stop}}{Ld}\right) \tag{1}$$

with $\theta_1$ the angle where $h_{stop}(\theta)$ diverges, $\theta_2$ the angle where $h_{stop}(\theta)$ vanishes, and $L$ a characteristic length scale. The values of the deposits $h_{stop}$ are determined by keeping the angle constant, and gradually decreasing the height $h$, i.e. the system size $N$. The deposit $h_{stop}$ is defined as the height at which the system jams and flow ceases upon reducing $h$ back down: in this case, only a few particles at the free surface rearrange, but this does not lead to a bulk motion [13, 14].

In Fig. 3, the stability diagram is represented in the vibration-free case $\Gamma = 0$ and for $\Gamma = 0.21$. In the vibration-free case, the simulations data points are well fitted to Eq. 1. The fitting parameters are $\theta_1 = 20.92^\circ$, $\theta_2 = 33.56^\circ$, and $L \approx 4.73$. In the following, we define $\theta_1$ in the vibration-free case as $\theta_c$ the critical angle below which no flow can occur without the addition of an external energy. In Fig. 3(inset), the deposits are plotted as a function of the rescaled angle $\theta/\theta_1$ for our DEM simulations and experimental data extracted from Gaudel *et al.* [22], with $\theta_{1_{exp}} = 24.7^\circ$, and $d/\lambda = 1/3$. The discrepancy concerning the value of $\theta_c$ may be attributable to the diameter of the particles: in experiments, beads of hundred microns are humidity-sensitive, increasing the cohesion between them. In our DEM simulations, the cohesion is not taken into account. Except this, results from DEM simulations are in good agreement with experimental data.

The value of $h_{stop}$ decreases with increasing $\Gamma$, for a given angle $\theta$ (Fig. 3). The Eq. 1 gives $\theta_1 = 20.47^\circ$, $\theta_2 = 32^\circ$, and $L \approx 2.19$. Hence, the minimum angle at which flow occurs decreases when vibration intensity increases. The vibrations affect the system by flowing a particle thickness $(h_{stop_{NV}} - h_{stop})$, where $h_{stop_{NV}}$ is the thickness of the deposits with no applied vibration and $h_{stop}$ is the thickness of the deposits [22].

The results obtained in DEM simulations are in agreement with those ob-

tained in experiments. We thus can define two regimes separated by a critical angle $\theta_c$, whose value depends on the properties of the granular system studied. Above $\theta_c$, this is a gravity-driven regime. Below this angle, no flow can occur without adding vibrations: it is a vibration-driven regime. In the following sections, we study in detail depth profiles and propose scaling laws in the two regimes, considering the effect of the vibrations.

### *3.2. Gravity-driven regime*

#### *3.2.1. Depth profiles*

***Stress ratio***. Depth profiles as functions of $z/d$ are computed for the normal stress ratio $\sigma_{zz}/\sigma_{xx}$ (Fig. 4(a)) and the shear stress ratio $\sigma_{zx} = \sigma_{zz}$ (Fig. 4(b)) for various inclinations angles and $N = 112500$. The normal stress ratio is close to one at intermediate values of the incline angle. The normal stress ratio is no longer one for high values of $\theta$ because kinetic contribution becomes more important than the frictional one. However, when $\theta$ is near the avalanche angle, there are large fluctuations in the contact network because flows are very slow (creep flow). Indeed, large fluctuations in the normal stress appear. The shear stress ratio equals $\tan(\theta)$, except at the bottom and the surface of the flow (i.e. the boundaries), as predicted in the framework of $\mu(I)$ [6, 8].

***Solid packing fraction***. Depth profiles of the solid packing fraction $\phi$ are computed for $\theta = 28°$ and different values of system sizes $N$ (Fig. 4(c)). The profiles exhibit no significant variation with depth throughout the bulk. The mean value of $\phi$ in the bulk is the same for a given $\theta$, whatever the system size, as expected for thick systems [10, 14]. Moreover, the profiles are exactly the same even when vibrations are applied for a given system size $N$. However, the mean value of $\phi$ decreases with the slope (Fig. 4(d)) due to a growing dilatant region near the free surface (i.e. a lower packing fraction), as already observed

in previous studies [10, 14, 33]. Our data are well fitted to the relation proposed by Ertas *et al.* [33] in the 3D case:

$$\phi(\theta) = \phi_{max} - c_{3D}\,(\theta - \theta_c) \tag{2}$$

with the imposed value $\phi_{max} = 0.595$, and the fitted value $c_{3D} = 0.009$.

***Velocity profiles***. Bagnold [34, 35] proposed a simple 2D model describing the collisional process between particle layers during granular flow. The relations predict a shear stress proportional to the square of the shear rate:

$$\sigma \propto \dot{\gamma}^2, \text{ with } \dot{\gamma} = \frac{\partial v_x(z)}{\partial z} \tag{3}$$

In a local and Newtonian case, we typically use the relationship $\sigma = \eta\dot{\gamma}$, with $\eta$ a viscosity. If Bagnold's argument is applied to the case of bulk granular flow, with no-slip condition at the base, the velocity depth-profile is such as:

$$v_x(z) \propto \left[h^{3/2} - (h-z)^{3/2}\right] \tag{4}$$

for a system size $N$ of total height $h$, where $z$ is measured from the bottom of the stack. The velocity profiles are plotted in Fig. 5(a), for various $\theta$, system sizes $N$, and $\Gamma$ values. In the following, the flow velocity is denoted $v_x = v$. As expected, all the velocity profiles are well fitted to a Bagnold profile (Eq. 4).

In the $\mu(I)$ framework, the main results are retrieved: (i) for a given angle $\theta$ and a given $\Gamma$ value, the velocity increases with increasing the system size $N$ and (ii) for a given system size $N$, the velocity increases with increasing the tilt angle.

Nevertheless, for a given $\theta$ and a given system size $N$, increasing the $\Gamma$ value does not change the profile nor the values of the velocity. This observation

suggests that the local law $\mu(I)$ is not impacted by the vibrations in the steady-state.

***Rheology.*** We present here results obtained for $\Gamma = 0.21$ which is the maximum value of the relative acceleration used in this regime in accordance with the experiments.[3] Given this, we have plotted the evolution of the shear stress with $z$ in Fig. 5(b), only for the free-vibration case. The local values of the shear rate are obtained by deriving the raw data of the velocity profile, as defined in Eq. 3. From these results, the flow curves are plotted for various systems (Fig. 5(c)), allowing us to check the assumption of a Bagnold rheology (Eq. 3).

However, there is a transition away from this Bagnold rheology as the stack becomes thinner. Indeed, the data in the case $\theta = 28^\circ$ and $N = 12500$, i.e. thin pile ($h \mapsto h_{stop}$), are well fitted to a linear profile. This leads to an increase of the strain rate near the surface. This behavior has already been observed and may be explained by the emergence of nonlocal effects, resulting from competing length scales in these thin piles [2, 5, 14, 36].

***Deposits.*** To go further, the evolution of the deposits with respect to the $\Gamma$ value is studied. To properly compare results obtained by DEM simulations and those by experiments, the evolution of the deposits is plotted as a function of $\Gamma/\Gamma_c$ (Fig. 6), where $\Gamma_c$ is defined as the critical relative acceleration for which $h_{stop}$ vanishes, and for the same value of $\theta/\theta_c$. These results are in agreement with the observations in experiments [22]. Indeed, adding vibrations in the gravity-driven regime only modifies the values of the deposits, not the dynamics in the steady-state regime.

#### *3.2.2. Velocity scaling*

Pouliquen have shown in experiments that granular flows down inclines obey a simple scaling relation [1], which was checked in many experimental and nu-

merical studies:

$$\mathrm{Fr} = \frac{v}{\sqrt{gh}} \propto \beta \frac{h}{h_{stop}(\theta)} \tag{5}$$

where $\beta = 0.136$ is a fitted coefficient, and the dimensionless Froude number is the ratio of the mean velocity and a velocity of reference $\sqrt{gh}$, with $g$ the gravity and $h$ the height of the grains pile.

Our recent study about granular avalanches down rough and vibrated inclines put in evidence that vibrations affect the apparent scaling law, leading to the following relation [22]:

$$\mathrm{Fr} = \frac{v}{\sqrt{gh}} = \tilde{\beta} \left( \frac{h}{h_{stop}^{eff}(\theta)} - 1 \right) \tag{6}$$

where $\tilde{\beta}_{exp} \simeq 0.1$, and $h_{stop}^{eff}(\theta) = h_{stop_{NV}}(\theta) \times d/\lambda$ is an effective stopping height defined as the product of the height of the deposits for a given tilt angle when no vibration are applied, and the relative roughness. In Fig. 7(inset), the ratio of the mean velocity $v$ over the surface velocity $v_s$ is plotted as a function of $h/h_{stop}^{eff}$, for DEM simulations and experimental results. This ratio is about $v/v_s \simeq 0.6$, in agreement with a Bagnold rheology, and falls when $h \mapsto h_{stop}$ due to nonlocal effects.

The evolution of $v_s/\sqrt{gh}$ is plotted as a function of $h/h_{stop}^{eff}$ (Fig. 7) for DEM simulations and experimental results extracted from Gaudel *et al.* [22]. All the data points collapse on the same straight line which confirms that the influence of the bead size $d$, the tilt angle $\theta$, and the roughness condition $\lambda$, are included in the single function $h_{stop}^{eff}$. The data are well fitted to $v_s/\sqrt{gh} = 0.18 \times \left( h/h_{stop}^{eff} - 1 \right)$. Taking into account the value of the ratio $v/v_s$, it leads to the scaling law of Eq. 6, with $\tilde{\beta}_{simu} = 0.108$. This value is in good agreement with the experimental result $\tilde{\beta}_{exp}$ obtained in the case of vibrated inclines, and also with $\beta$ determined by Pouliquen.

The scaling law (Eq. 6), derived from the scaling relation proposed by Pouliquen (Eq. 5), appears to be robust to predict flow properties of granular flows, even under vibrations. However, when the gravity is not sufficient to trigger the flow, i.e. in the vibration-driven regime, the apparent scaling law is changed.

### *3.3. Vibration-driven regime*

In this section, we are interested in the vibration-driven regime, i.e. $\theta < \theta_c$ where the flow is induced by vibrations. For the first time, we explore the behavior of granular flows in this regime only for $\theta = 20°$. In the range of 0.02 to 0.21 of $\Gamma$ values, granular flows occur but velocity profiles are linear. In order to understand the dynamics due to vibrations in this regime, velocity profiles presented in this section are obtained for $\Gamma$ values in the range 2.13 to 6.40. For this range of vibrations, no experiment have been performed due to experimental constraints. The following results are thus only obtained by DEM simulations.

#### *3.3.1. Depth profiles*

***Stress profiles and solid packing fraction***. Depth profiles as functions of $z/d$ are computed for the normal stress ratio $\sigma_{zz}/\sigma_{xx}$, the shear stress ratio $\sigma_{zx}/\sigma_{zz}$, and for the solid packing fraction $\phi$ (Fig. 8(a) and (b), respectively), for various system sizes $N$ and $\Gamma$ values, and for $\theta = 20°$. One can make the same remarks as in the gravity-driven regime (*cf* Section 3.2.1): the normal stress ratio equals one and the shear stress ratio equals $\tan(\theta)$, except at the bottom and the surface of the flow (i.e. the boundaries). The depth profiles exhibit no significant variation with depth throughout the bulk, and the mean value of $\phi$ in the bulk is the same for a given $\theta$, whatever the system size $N$. It dismisses the assumption of a plug flow that would be created by the vibrations,

otherwise we shall observe an abrupt change in the volume fraction with height, denoting the interface between the flowing and the plug regions [37, 38]. The bulk value of $\phi$ keeps constant with the $\Gamma$ value, and seems to have reached its maximal value $\langle\phi\rangle = 0.59$ (Fig. 8(d)), in agreement with the expected value of $\phi_{max}$ (Eq. 2).

***Rheology***. The depth profiles of the shear stress are plotted for $\theta = 20^\circ$ and various system sizes $N$ and $\Gamma$ values (Fig. 9(a)). The shear stress is linear with the depth and only depends on the system size, as already observed in the regime $\theta < \theta_c$ (*cf* Fig. 5(b)). However, the flow curves presented in Fig. 9(b) differ from the case gravity-driven regime. Actually, the shear stress seems to be proportional to the square root of the shear rate $\sigma \propto \dot{\gamma}^{1/2}$.

***Velocity profiles***. This difference comes from a velocity profile which is not of the Bagnold form anymore (Fig. 9(c)).

In general, for a given $\Gamma$ value, the velocity decreases with increasing the system size $N$.

And for a given value of $N$, the velocity increases with increasing $\Gamma$. These behavior can be explained by an increase of the particle mobility, all the more important that the energy of vibrations provided to each particle is high.

The velocity profiles exhibit an exponential form, with a fast increase of the velocity near the bottom of the plane before reaching a quasi constant value. This kind of behavior has already been observed, in flow of upper-convected Maxwell fluid over a plate [39, 40], or also in creeping flows down planes [4, 41]. Most particularly, this behavior has been put in evidence in flows of a 2D granular bed close to the jamming transition (i.e. for $I \leq 2 \times 10^{-2}$) by Staron

*et al.* [9], and the velocity profile is given by:

$$\frac{v(z)}{\sqrt{gd}} = \frac{v_s/\sqrt{gd}}{1-\exp\left(-\frac{H/d}{\xi/d}\right)}\left[1-\exp\left(-\frac{z/d}{\xi/d}\right)\right] \tag{7}$$

with $v_s = v(z = H)$ depending on the vibration intensity and the system size, and $\xi$ a characteristic length.

The evolution of this dimensionless characteristic length $\xi/d$ is plotted as a function of the acceleration of the vibrations $\Gamma$ for various system sizes $N$ (Fig. 10, blue markers). The value of $\xi/d$ can be considered as a constant for a given $\Gamma$ value, whatever the system size. However, this value decreases with increasing the intensity of vibrations, and seems to be an inverse function of $\Gamma$ such as $\xi/d \propto 1/\Gamma$. An interpretation of this characteristic length is proposed in the next section 3.3.2. In this figure, the case $N = 37500$ is not presented because the data do not collapse on the others. A possible explanation is that, for thin systems, confinement effects are expected to become significant. This would need to be established in further work.

### *3.3.2. Velocity scaling*

Staron *et al.* [9] propose that, in the case of an exponential profile for the velocity, the shear rate is actually a function of the granular temperature $T$. The granular temperature is defined as the square of the mean particles velocity fluctuations:

$$T(z) = \langle \delta v^2 \rangle = \langle \delta v_x^2(z) + \delta v_y^2(z) + \delta v_z^2(z) \rangle \tag{8}$$

The rescaled shear rate is plotted as a function of the rescaled granular temperature in Fig. 11, for $\theta = 20°$ and various values of $N$ and $\Gamma$. The collapse of all data on the same master curve over several orders of magnitude is suitable

for a power-law, and the best fit is given by:

$$\dot{\gamma}(z)\sqrt{\frac{d}{g}} = \alpha \times \left(\frac{T(z)}{gd}\right)^{\beta} \tag{9}$$

with $\alpha = 1.33$ and $\beta = 2/3$. This scaling and the values of $\alpha$ and $\beta$ are in agreement with previous observations of grains dynamics in granular bed flows [9], in simulated plan shear flows [42], and in annular shear configurations [43]. This result strongly suggests a nonlocal behavior.

This scaling also implies that an exponential decay is a good approximation for the decrease of the temperature along the $z-$ direction. Since the derivative of the Eq. 7 has to be equal to the expression of the shear rate in Eq. 9, the depth temperature profile is given by:

$$\frac{T(z)}{gd} \propto \frac{T_0}{gd} \exp\left(-\frac{z}{\beta\xi}\right) \tag{10}$$

with $T_0$ a constant depending on the value of $\Gamma$. The depth profiles of the granular temperature are plotted in Fig 12. Except close to the boundaries, the data are well fitted to the above relation (Eq. 10). This confirms the scaling law proposed in Eq. 9.

However, the origin of the higher temperature at the bottom and its exponential decrease is still not clear. In this paper, we make the assumption that the exponential profile would come from the damping of the waves created by the vibrations. In our work, transverse vibrations are imposed to the granular system at the bottom of the plane. We thus propose to draw an analogy with the flow of a viscoelastic fluid close to a plane oscillating transversely. In this case, the velocity parallel to the plane, i.e. $v_y$, verifies:

$$v_y(z,t) = f(z)\cos(\omega t + \varphi) = \Re\left(f(z)e^{i\omega t}\right) \tag{11}$$

with $f(z)$ a function of the depth $z$, $\omega$ a typical frequency, and $\varphi$ the phase offset.

The velocity $v_y$ is plotted with respect to $z$ at different times for a typical simulation (Fig. 13(a)). For one period of vibration defined as $T = 1/f$, the mean values of the velocity in time and in space are equal to zero. The parallel velocity propagates along the $z-$ direction with damping oscillations. Indeed, the vibrations propagate in the bulk and are dissipated at each layer of particles. The function describing the oscillations seems to be of the form of Eq. 11 but there is a change in the period of the oscillations: it decreases with $z$. An example is represented in Fig. 13(a), and the observation is exactly the same for all our DEM simulations. This may come from a coupled effect with the gravity but further investigations are necessary to obtain this information. In all cases, it is well known that the dissipative mechanism of the system is included in the damping coefficient extracted from the exponentially decaying envelope:

$$\frac{v_y(z)}{\sqrt{gd}} \propto \gamma \exp\left(-\kappa \frac{z}{d}\right) \tag{12}$$

with $\gamma$ a constant depending on the parameters of the simulation, and $\kappa$ the damping coefficient. A typical example is plotted in Fig. 13(b). The damping coefficient is extracted for each simulation, i.e. for $\theta = 20^\circ$, all system sizes and $\Gamma$ values studied. This damping coefficient can be defined as the inverse of a penetration depth of the parallel velocity $\kappa^{-1} = \delta/d$, meaning the penetration depth of the vibrations in the bulk. Taking into account that the granular temperature is actually created by the vibrations, it should exist a relation of proportionality between $T(z)$ and $v_y(z)$. This directly leads to the fact that $\delta/d = \beta\xi/d$. Hence, the evolution of the extracted penetration depth $\delta/\beta d$ is plotted as a function of the intensity of the vibrations $\Gamma$ for $\theta = 20^\circ$ and various values of $N$ (Fig. 10, red markers). The data collapse on the same master curve

and $\delta/d$ seems to be an inverse function of $\Gamma$ in the range of values studied here. The waves propagate more efficiently than the intensity of vibrations is high. Moreover, the values of $\delta/\beta d$ extracted from the exponential envelopes are the same than the values of $\xi/d$ extracted from the velocity profiles. These results validate our assumption, and point at the velocity fluctuations due to the vibrations at the bottom as the agent allowing for nonlocality. The vibrations create fluctuations that enable rearrangements at the grain scale, all the more important that $\Gamma$ is high, and thus unjammed the system.

## 4. Conclusions

In order to test the influence of vibrations on free surface granular flows, we have performed particle-based DEM numerical simulations of stationary chute flows, for a large range of vibration intensities and inclination angles. As expected in the phase-diagram (Fig. 1), adding vibrations allows flow under the angle of avalanche and modifies the transition between the jammed and the unjammed regime. We identify two regimes, in agreement with experimental results.

A gravity-driven regime appears for angles larger than the angle of avalanche, where a collisional rheology is recovered at no variation and various vibration intensities. Vibrations modify the depth of the deposits and thus the apparent rheology. All data can be rationalized by introducing an effective deposit length $h_{stop}^{eff}$.

Below the angle of avalanche, stationary flows can be obtained by applying controlled vibrations. In this vibration-driven regime, the Bagnold rheology fails and exponential velocity profiles are obtained. We show that the rheology in this regime is related to an exponential profile of the granular temperature along the depth of the granular packing. A characteristic length scale appears which

is directly related to the damping factor of transverse vibrations waves. These waves propagate in the bulk of the packing and make the rheology nonlocal, with $\dot{\gamma}(z) \propto T(z)^{2/3}$. This scaling is in agreement with results previously obtained in the literature when $I \mapsto 0$, where velocity fluctuations control the rheology.

In a future work, it could be of interest to perform more simulations in order to obtain the relationship between the minimum relative acceleration necessary to trigger the flow and the inclination angle.

## Acknowledgments

This study is conducted in the framework of the "PowderReg" project, funded by the European programme Interreg VA GR within the priority axis 4 "Strengthen the competitiveness and the attractiveness of the Grande Région / Großregion". The authors thank F. Qi (University of Luxembourg) for fruitful discussions and for his wise advice.

## Appendix A Description of the model

In this paper, the contact model used in the DEM simulations is a Hertzian-Mindlin model, with friction, rolling, and dissipation, but with no cohesion [23, 25, 29, 30]. For two grains in contact of diameter $d$ and mass $m$ separated by a distance $r$, the normal direction $\mathbf{n}$ is defined as the line connecting them centers, and the tangential one $\mathbf{t}$ is in the plane perpendicular to $\mathbf{n}$. The contact force $\mathbf{F_c}$ is then zero when $r > d$. When $r < d$, one can define the normal overlap $\delta_n = d - r$, and the tangential one $\delta_t$ corresponding to the relative displacement of the grains from the onset of the contact. The force is then decomposed in its normal and tangential parts, $\mathbf{F_n}$ and $\mathbf{F_t}$, respectively:

$$
\begin{aligned}
\mathbf{F_c} &= \mathbf{F_n} + \mathbf{F_t} \\
\mathbf{F_n} &= k_n \delta_n \mathbf{n} + \gamma_n \mathbf{v_n} \\
\mathbf{F_t} &= k_t \delta_t \mathbf{t} + \gamma_t \mathbf{v_t} \qquad \text{, if } |F_t| \leq \mu |F_n| \\
&= \mu |F_n| \qquad\qquad\qquad \text{, else}
\end{aligned}
$$

where $\mathbf{v_n}$ and $\mathbf{v_t}$ are the normal and the tangential components of the relative velocity of the particles and $\mu$ is the friction coefficient. The normal and tangential stiffness $k_n$ and $k_t$, and the damping coefficients $\gamma_n$ and $\gamma_t$ are defined in Tab. 1.

Concerning the calculation of the rolling coefficients, a rolling torque resistance model for spherical particles is applied. This model applies a constant directional torque on two particles in contact, depending on their rotational velocity [27, 44, 45]:

$$\mathbf{M}_\mu = \mu_r \frac{d}{4} \mathbf{F_n} \frac{\omega_r}{|\omega_r|}$$

where $\mathbf{M}_\mu$ is the frictional torque, $\mu_r$ is the rolling friction coefficient and $\omega_r$ is the relative rotating velocity.

## Appendix B Summary table presenting the performed simulations

Here is presented a summary of the simulations that have been performed in this paper, with their properties (Tab. 2).

## Notes

[1]In order to compare DEM simulations and experimental results presented in Ref. [22], a range of vibration amplitudes is selected for DEM simulations, ensuring the same kinetic energy $E_k$ by grains in both cases:

$$E_{k_{DEM}} = E_{k_{EXP}} \Leftrightarrow m_{g_{DEM}} (Af)^2_{DEM} = m_{g_{EXP}} (Af)^2_{EXP}$$

where $m_g$ is the mass of one grain defined as $m_g = 4/3\pi R^3 \rho$, with $R$ the radius and $\rho$ the density of the particle under consideration. For instance, we used glass beads in experiments

($\rho = 2500$ kg/m$^3$) with a diameter $d = 100$ µm, submitted to a frequency $f = 30$ Hz, and a range of amplitude of vibrations $A_{EXP} = [0.5 \text{ to } 4]\, d$, the order of magnitude of the amplitude of vibrations that has to be used in DEM simulations is then $A_{DEM} = [0.001 \text{ to } 0.01]\, d$.

[2]The study of the propagation of the vibrations along the $z-$direction requires a large dimension size in the $y-$direction, i.e. along the vibrations direction.

[3]We have checked that these results remain fair for $\Gamma < 0.21$.

## References


[1] O. Pouliquen, Scaling laws in granular flows down rough inclined planes, Physics of Fluids 11 (3) (1999) 542–548. doi:10.1063/1.869928.

[2] F. Malloggi, B. Andreotti, E. Clément, Nonlocal effects in sand flows on an inclined plane, Physical Review E 91 (5) (2015) 052202. doi:10.1103/PhysRevE.91.052202.

[3] R. Artoni, A. Santomaso, Effective wall slip in chutes and channels: experiments and discrete element simulations, Granular Matter 16 (3) (2014) 377–382. doi:10.1007/s10035-013-0431-y.

[4] P. Jop, Y. Forterre, O. Pouliquen, Initiation of granular surface flows in a narrow channel, Physics of Fluids 19 (8) (2007) 088102. doi:10.1063/1.2753111.

[5] S. Deboeuf, E. Lajeunesse, O. Dauchot, B. Andreotti, Flow rule, self-channelization, and levees in unconfined granular flows, Physical review letters 97 (15) (2006) 158303. doi:10.1103/PhysRevLett.97.158303.

[6] G. D. R. MiDi, On dense granular flows, The European Physical Journal E 14 (4) (2004) 341–365. doi:10.1140/epje/i2003-10153-0.

[7] C. Ancey, Dry granular flows down an inclined channel: Experimental investigations on the frictional-collisional regime, Physical Review E 65 (1) (2001) 011304. doi:10.1103/PhysRevE.65.011304.

[8] R. Artoni, A. C. Santomaso, M. Go, P. Canu, Scaling laws for the slip velocity in dense granular flows, Physical review letters 108 (23) (2012) 238002. doi:10.1103/PhysRevLett.108.238002.

[9] L. Staron, P.-Y. Lagrée, C. Josserand, D. Lhuillier, Flow and jamming of a two-dimensional granular bed: Toward a nonlocal rheology?, Physics of Fluids 22 (11) (2010) 113303. doi:10.1063/1.3499353.

[10] L. Staron, Correlated motion in the bulk of dense granular flows, Physical Review E 77 (5) (2008) 051304. doi:10.1103/PhysRevE.77.051304.

[11] O. Baran, D. Ertaş, T. C. Halsey, G. S. Grest, J. B. Lechman, Velocity correlations in dense gravity-driven granular chute flow, Phys. Rev. E 74 (2006) 051302. doi:10.1103/PhysRevE.74.051302.

[12] G. Lois, A. Lemaître, J. M. Carlson, Numerical tests of constitutive laws for dense granular flows, Phys. Rev. E 72 (2005) 051303. doi:10.1103/PhysRevE.72.051303.

[13] L. E. Silbert, J. W. Landry, G. S. Grest, Granular flow down a rough inclined plane: Transition between thin and thick piles, Physics of Fluids 15 (1) (2003) 1–10. doi:10.1063/1.1521719.

[14] L. E. Silbert, D. Ertaş, G. S. Grest, T. C. Halsey, D. Levine, S. J. Plimpton, Granular flow down an inclined plane: Bagnold scaling and rheology, Phys. Rev. E 64 (2001) 051302. doi:10.1103/PhysRevE.64.051302.

[15] D. M. Hanes, O. R. Walton, Simulations and physical measurements of glass spheres flowing down a bumpy incline, Powder technology 109 (1-3) (2000) 133–144. doi:10.1016/S0032-5910(99)00232-6.

[16] N. Gaudel, S. Kiesgen de Richter, N. Louvet, M. Jenny, S. Skali-Lami, Bulk

and local rheology in a dense and vibrated granular suspension, Phys. Rev. E 96 (2017) 062905. doi:10.1103/PhysRevE.96.062905.

[17] S. K. de Richter, C. Hanotin, P. Marchal, S. Leclerc, F. Demeurie, N. Louvet, Vibration-induced compaction of granular suspensions, The European Physical Journal E 38 (7) (2015) 74. doi:10.1140/epje/i2015-15074-7.

[18] C. Hanotin, S. Kiesgen de Richter, L. J. Michot, P. Marchal, Viscoelasticity of vibrated granular suspensions, Journal of Rheology 59 (1) (2015) 253–273. doi:10.1122/1.4904421.

[19] R. Capozza, A. Vanossi, A. Vezzani, S. Zapperi, Triggering Frictional Slip by Mechanical Vibrations, Tribology Letters 48 (1) (2012) 95–102. doi:10.1007/s11249-012-0002-0.

[20] S. Kiesgen de Richter, G. Le Caër, R. Delannay, Heterogeneous dynamics of a granular pack under vertical tapping, EPL (Europhysics Letters) 85 (5) (2009) 58004. doi:10.1209/0295-5075/85/58004.

[21] P. Richard, P. Philippe, F. Barbe, S. Bourlès, X. Thibault, D. Bideau, Analysis by x-ray microtomography of a granular packing undergoing compaction, Phys. Rev. E 68 (2003) 020301. doi:10.1103/PhysRevE.68.020301.

[22] N. Gaudel, S. Kiesgen de Richter, N. Louvet, M. Jenny, S. Skali-Lami, Granular avalanches down inclined and vibrated planes, Phys. Rev. E 94 (2016) 032904. doi:10.1103/PhysRevE.94.032904.

[23] P. Cundall, O. Strack, A discrete numerical model for granular assemblies, Geotechnique 29 (1) (1979) 47–65.

[24] C. Goniva, C. Kloss, A. Hager, S. Pirker, An open source CFD-DEM perspective, Proceedings of OpenFOAM Workshop, Göteborg (2010) 1–10.

[25] C. Kloss, C. Goniva, A. Hager, S. Amberger, S. Pirker, Models, algorithms and validation for opensource DEM and CFD-DEM, Progress in Computational Fluid Dynamics, An International Journal 12 (2/3) (2012) 140. doi:10.1504/PCFD.2012.047457.

[26] F. Guillard, Y. Forterre, O. Pouliquen, Lift forces in granular media, Physics of Fluids 26 (4) (2014) 043301. doi:10.1063/1.4869859.

[27] Y. Zhou, B. Xu, A. Yu, P. Zulli, An experimental and numerical study of the angle of repose of coarse spheres, Powder Technology 125 (1) (2002) 45 – 54. doi:10.1016/S0032-5910(01)00520-4.

[28] P. Frankowski, M. Morgeneyer, Calibration and validation of DEM rolling and sliding friction coefficients in angle of repose and shear measurements, 2013, pp. 851–854. doi:10.1063/1.4812065.

[29] R. Mindlin, Elastic spheres in contact under varying oblique forces, Journal of Applied Mechanics 20 (1953) 327–344.

[30] A. Di Renzo, F. P. Di Maio, Comparison of contact-force models for the simulation of collisions in DEM-based granular flow codes, Chemical Engineering Science 59 (3) (2004) 525–541. doi:10.1016/j.ces.2003.09.037.

[31] O. Pouliquen, N. Renaut, Onset of granular flows on an inclined rough surface: dilatancy effects, Journal de Physique II 6 (6) (1996) 923–935. doi:10.1051/jp2:1996220.

[32] A. Daerr, S. Douady, Two types of avalanche behaviour in granular media, Nature 399 (6733) (1999) 241.

[33] D. Ertaş, G. S. Grest, T. C. Halsey, D. Levine, L. E. Silbert, Gravity-driven dense granular flows, EPL (Europhysics Letters) 56 (2) (2001) 214.

[34] R. A. Bagnold, Experiments on a Gravity-Free Dispersion of Large Solid Spheres in a Newtonian Fluid under Shear, Proceedings of the Royal Society A: Mathematical, Physical and Engineering Sciences 225 (1160) (1954) 49–63. doi:10.1098/rspa.1954.0186.

[35] R. A. Bagnold, The Flow of Cohesionless Grains in Fluids, Philosophical Transactions of the Royal Society A: Mathematical, Physical and Engineering Sciences 249 (964) (1956) 235–297. doi:10.1098/rsta.1956.0020.

[36] P. Mills, D. Loggia, M. Tixier, Model for a stationary dense granular flow along an inclined wall, EPL (Europhysics Letters) 45 (6) (1999) 733.

[37] R. Brewster, G. S. Grest, J. W. Landry, A. J. Levine, Plug flow and the breakdown of Bagnold scaling in cohesive granular flows, Physical Review E 72 (6) (2005) 061301. doi:10.1103/PhysRevE.72.061301.

[38] C. S. Campbell, C. E. Brennen, Chute flows of granular material: some computer simulations, Journal of applied mechanics 52 (1) (1985) 172–178.

[39] T. Hayat, Z. Abbas, M. Sajid, Series solution for the upper-convected Maxwell fluid over a porous stretching plate, Physics Letters A 358 (5-6) (2006) 396–403. doi:10.1016/j.physleta.2006.04.117.

[40] T. Hayat, Z. Abbas, M. Sajid, MHD stagnation-point flow of an upper-convected Maxwell fluid over a stretching surface, Chaos, Solitons & Fractals 39 (2) (2009) 840–848. doi:10.1016/j.chaos.2007.01.067.

[41] T. S. Komatsu, S. Inagaki, N. Nakagawa, S. Nasuno, Creep Motion in a Granular Pile Exhibiting Steady Surface Flow, Physical Review Letters 86 (9) (2001) 1757–1760. doi:10.1103/PhysRevLett.86.1757.

[42] N. Xu, C. S. O'Hern, L. Kondic, Stabilization of nonlinear velocity profiles

in athermal systems undergoing planar shear flow, Phys. Rev. E 72 (2005) 041504. doi:10.1103/PhysRevE.72.041504.

[43] W. Losert, L. Bocquet, T. C. Lubensky, J. P. Gollub, Particle dynamics in sheared granular matter, Phys. Rev. Lett. 85 (2000) 1428–1431. doi:10.1103/PhysRevLett.85.1428.

[44] Y. C. Zhou, B. D. Wright, R. Y. Yang, B. H. Xu, A.-B. Yu, Rolling friction in the dynamic simulation of sandpile formation, Physica A: Statistical Mechanics and its Applications 269 (2-4) (1999) 536–553. doi:10.1016/S0378-4371(99)00183-1.

[45] J. Ai, J.-F. Chen, J. M. Rotter, J. Y. Ooi, Assessment of rolling resistance models in discrete element simulations, Powder Technology 206 (3) (2011) 269–282. doi:10.1016/j.powtec.2010.09.030.

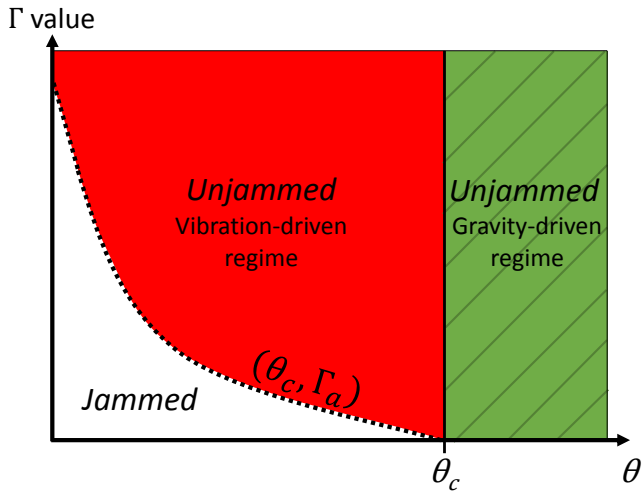


Figure 1: Hypothetical phase-diagram representing the influence of the vibrations on the jamming transition in gravitational granular flows. $\theta_c$ represents the critical angle below which no flow is possible without a minimum acceleration of vibrations $\Gamma_a$.

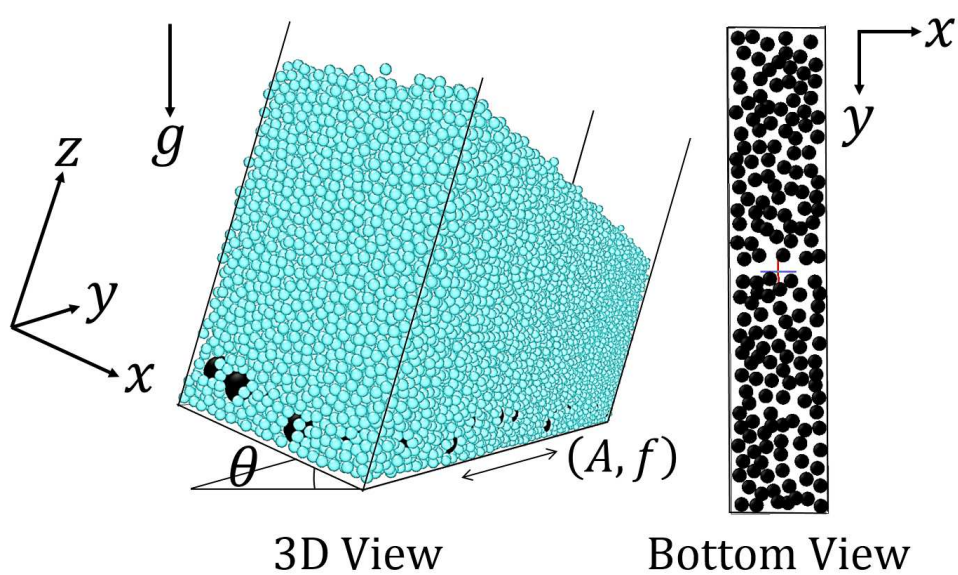


Figure 2: Typical snapshots from simulation, filled and empty box, (3D and bottom views) with a chute base area equals $20d \times 100d$, that is inclined at $\theta$ to the horizontal. The rough bed is fixed and denoted by dark particles of diameter $\lambda$. The flowing particles of diameter $d$ are in light color. Here, $d/\lambda = 1/3$, and $H/d \simeq 25$ corresponding to $N = 62500$ particles.

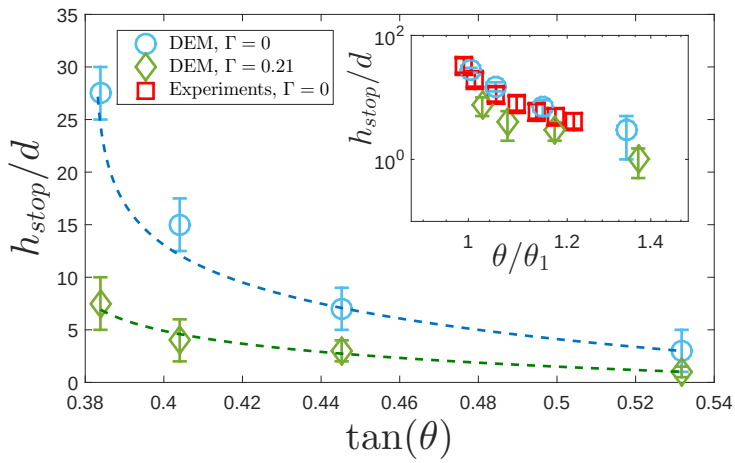


Figure 3: Stability diagram $h_{stop}/d - \tan(\theta)$ for granular chute flow in the vibration-free case ($\Gamma = 0$) and for $\Gamma = 0.21$. The dashed lines denote the flow line fit given by Eq. 1. Inset: rescaled stability diagram $h_{stop}/d - \theta/\theta_1$, with $\theta_1$ obtained through Eq. 1, for DEM simulations and experimental data extracted from Gaudel *et al* [22]. $\theta_1$ is the critical angle below which no flow occurs for a fixed value of $\Gamma$. All data correspond to a relative roughness $d/\lambda = 1/3$.

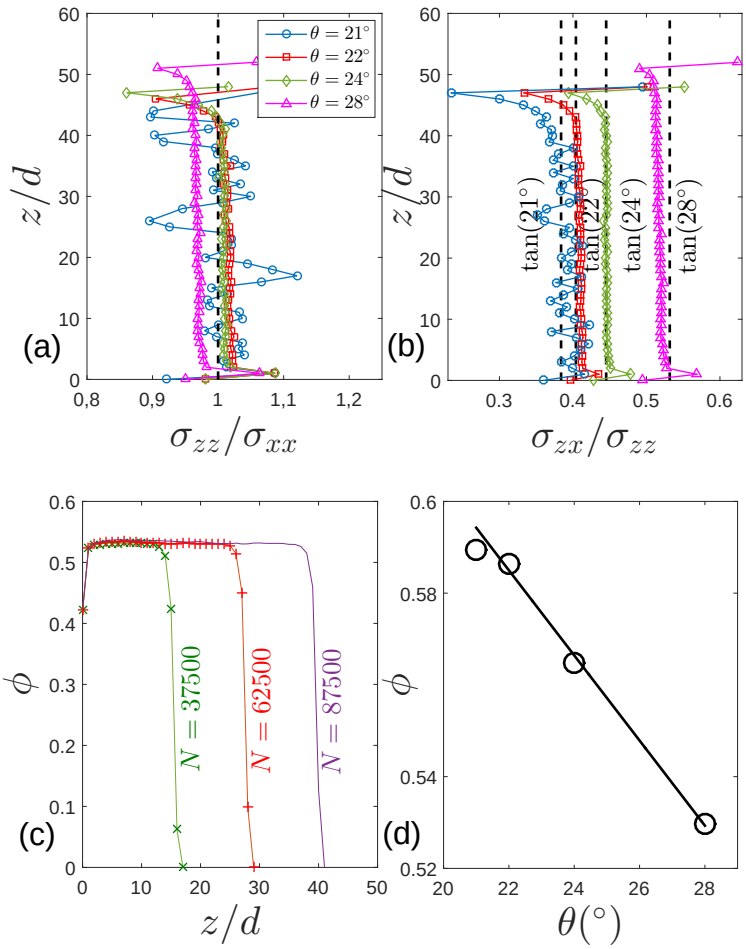


Figure 4: (a) Profiles of average normal stress ratio for $N = 112500$ and different values of $\theta$, the dashed line represents $\sigma_{zz} = \sigma_{xx}$. (b) Profiles of average shear stress ratio for $N = 112500$ and different values of $\theta$. (c) Depth profiles of the packing fraction for $\theta = 28°$ and different values of system sizes $N$, solid lines are data extracted for $\Gamma = 0$ and markers for $\Gamma = 0.21$. (d) Tilt dependence of the packing fraction, the solid line is fit to Eq. 2 [33]. All data correspond to a relative roughness $d/\lambda = 1/3$.

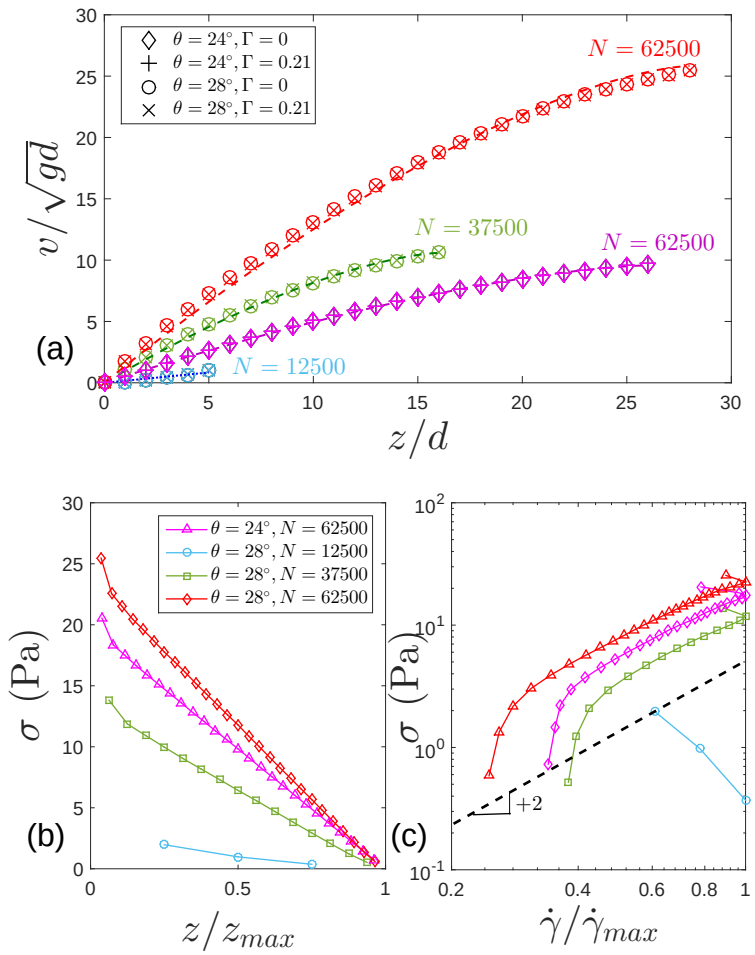


Figure 5: (a) Velocity profiles for various values of inclination $\theta$, system sizes $N$, and $\Gamma$. Markers are data extracted from DEM simulations and solid lines are fits to Bagnold profiles (Eq. 4), except for $N = 12500$ which is a linear fit. (b) Profiles of the shear stress $\sigma_{xz} = \sigma$ as functions of the normalized depth $z/d$, for various inclination angles $\theta$ and system sizes $N$. (c) Flow curves $\sigma - \dot{\gamma}$ for various inclination angles $\theta$ and system sizes $N$. The dashed line is a guide for the eyes: $\sigma \propto \dot{\gamma}^2$. All data correspond to a relative roughness $d/\lambda = 1/3$. For clarity, legend is the same for figures (b) and (c).

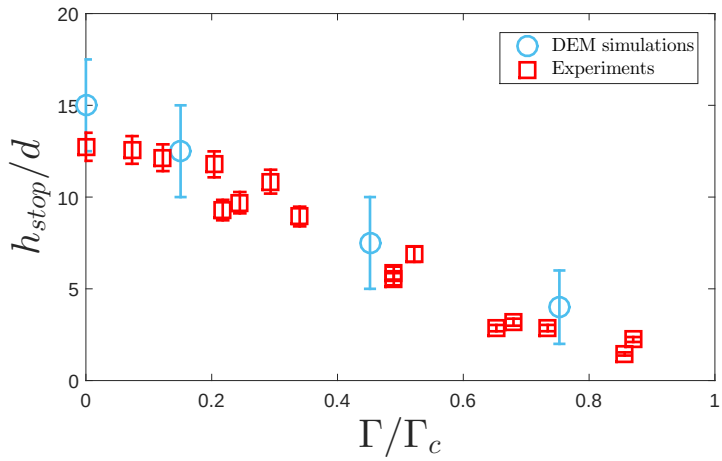


Figure 6: Evolution of $h_{stop}/d$ as a function of the rescaled relative acceleration $\Gamma/\Gamma_c$ for $\theta/\theta_c = 1.05$, for DEM simulations and experimental data extracted from Gaudel *et al* [22]. The values of $\Gamma_c$ for DEM and experiments are 0.28 and 1.48, respectively. All data correspond to a relative roughness $d/\lambda = 1/3$.

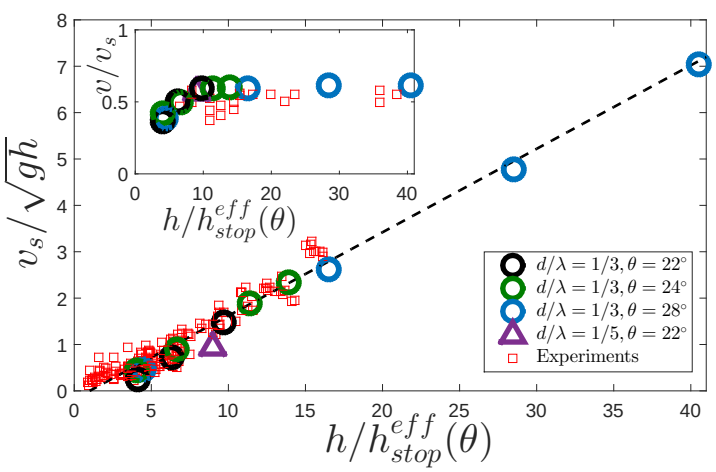


Figure 7: Froude number $v_s/\sqrt{gh}$ as a function of $h/h^{eff}_{stop}$ for DEM simulations and experimental data extracted from Gaudel *et al* [22]. The dashed line corresponds to the fit given by Eq. 6. Inset: Velocity ratio $v/v_s$ as a function of $h/h^{eff}_{stop}$, for the same data.

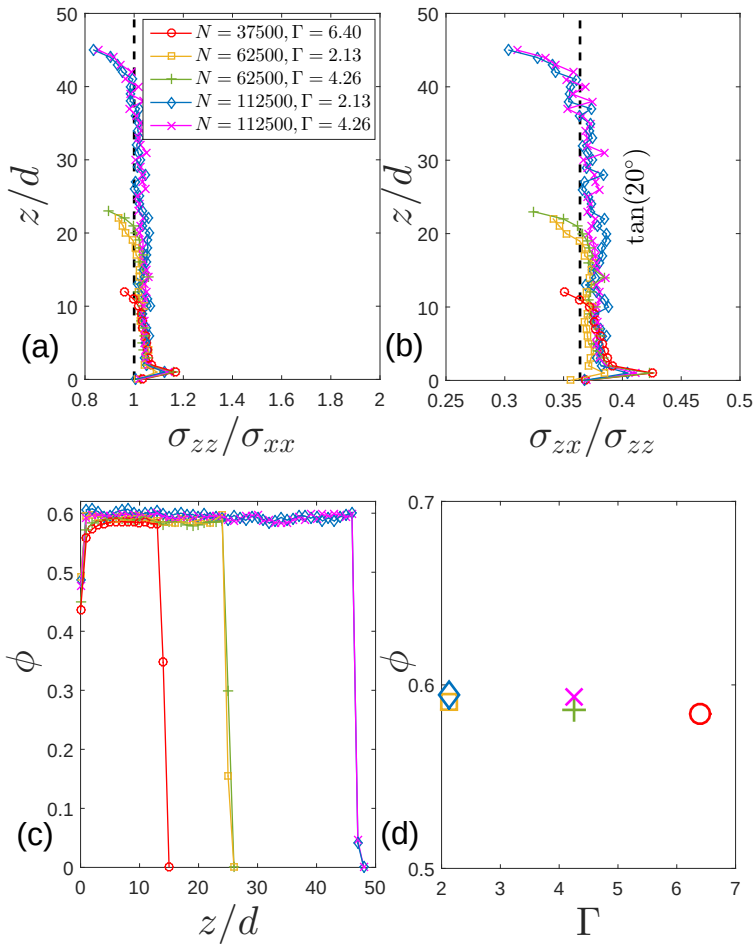


Figure 8: (a) Profiles of average normal stress ratio for $\theta = 20^\circ$ and different values of $N$ and $\Gamma$, the dashed line represents $\sigma_{zz} = \sigma_{xx}$. (b) Profiles of average shear stress ratio for $\theta = 20^\circ$ and different values of $N$ and $\Gamma$, the dashed line represents $\tan(20°)$. (c) Depth profiles of the packing fraction for $\theta = 20^\circ$ and different values of $N$ and $\Gamma$. (d) $\Gamma$ dependence of the packing fraction, for $\theta = 20^\circ$ and different values of $N$. All data correspond to a relative roughness $d/\lambda = 1/3$. For clarity, legend is the same for all figures.

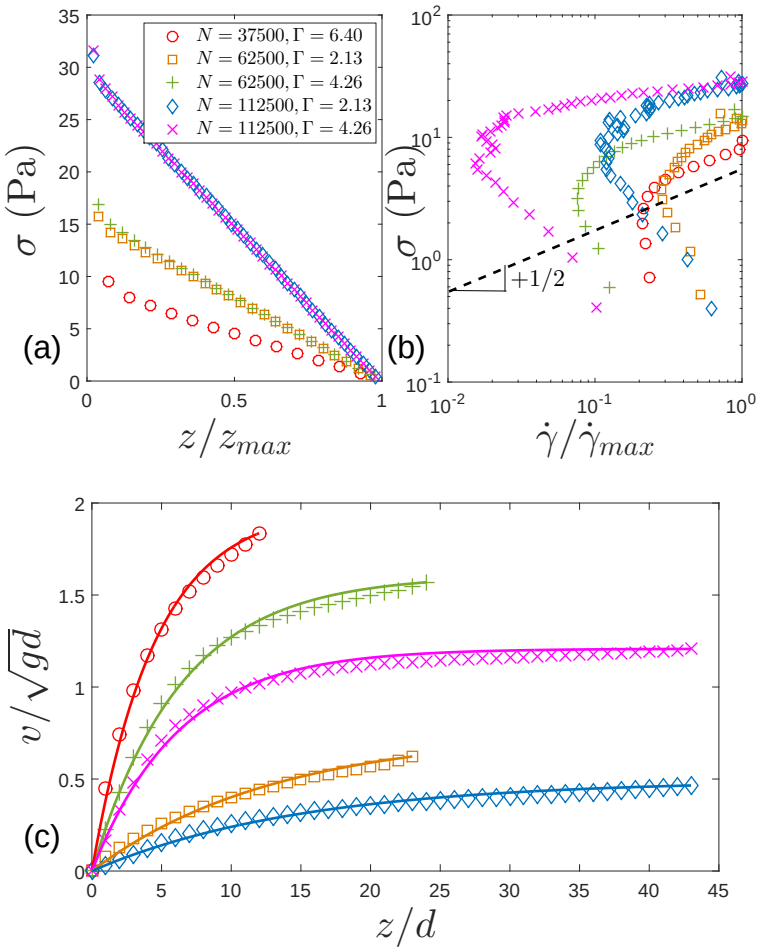


Figure 9: For $\theta = 20^{\circ}$ and for various $\Gamma$ values and system sizes $N$, (a) Profiles of the shear stress $\sigma_{xz} = \sigma$ as functions of the normalized depth $z/d$. (b) Flow curves $\sigma - \dot{\gamma}$. The dashed line is a guide for the eyes: $\sigma \propto \dot{\gamma}^{1/2}$. (c) Velocity profiles. Markers are data extracted from DEM simulations and solid lines are fits to exponential form (Eq. 7). All data correspond to a relative roughness $d/\lambda = 1/3$. For clarity, legend is the same for all figures.

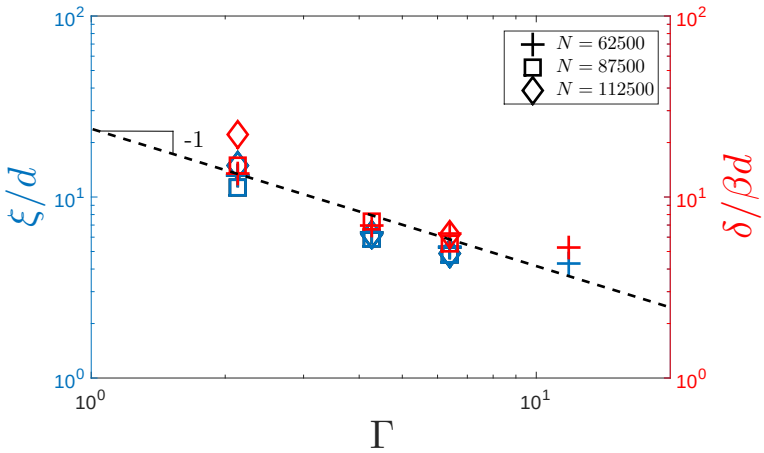


Figure 10: Evolution of the characteristic length $\xi/d$ (blue markers) and the penetration depth $\delta/\beta d$ (red markers) with respect to the value of $\Gamma$, for $\theta = 20^\circ$ and various system sizes $N$. All data correspond to a relative roughness $d/\lambda = 1/3$. The dashed line is a guide for the eyes: $\xi/d, \delta/d \propto 1/\Gamma$.

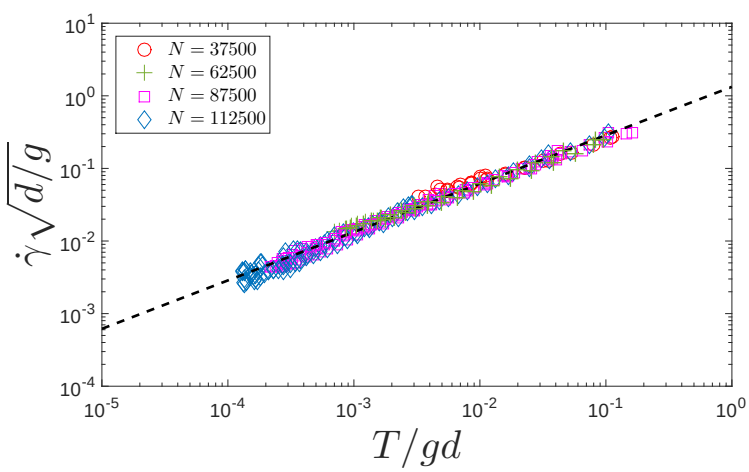


Figure 11: Local values of the normalized velocity gradient $\dot{\gamma}\sqrt{d/g}$ as a function of the normalized temperature $T/gd$, for $\theta = 20^\circ$, various system sizes, and various $\Gamma$ values. The dashed line shows the power-law trend $\dot{\gamma}\sqrt{d/g} = 1.33\,(T/gd)^{2/3}$. All data correspond to a relative roughness $d/\lambda = 1/3$.

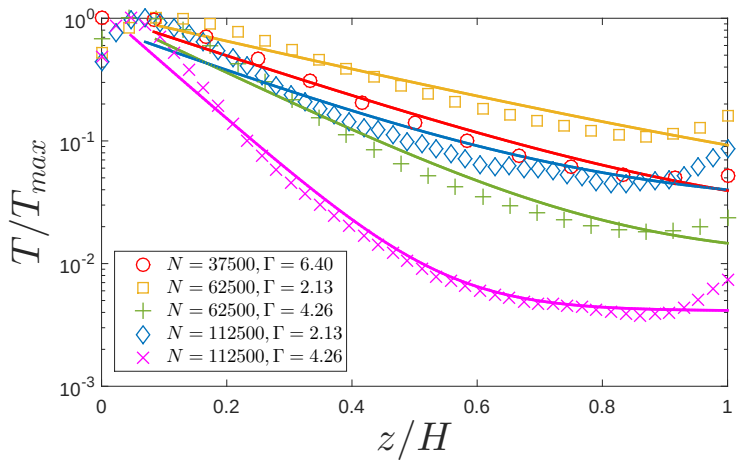


Figure 12: Normalized depth profiles of the granular temperature $T/T_{max}$ for $\theta = 20^\circ$ and different values of N and $\Gamma$. The solid lines show the fits given by Eq. 10. All data correspond to a relative roughness $d/\lambda = 1/3$.

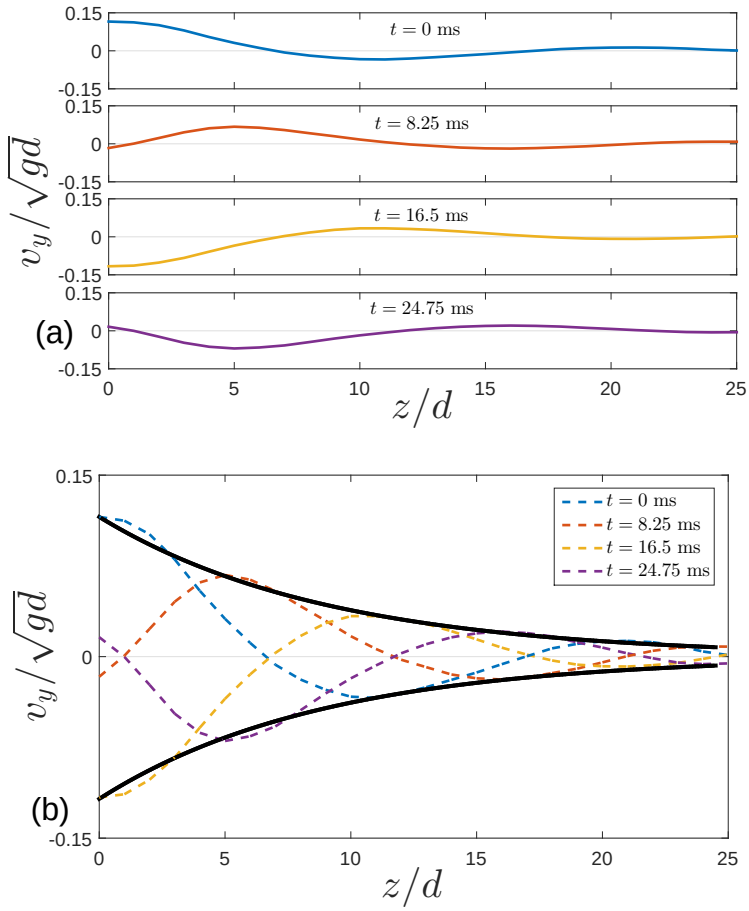


Figure 13: Evolution of the transverse velocity $v_y/\sqrt{gd}$ along $z/d$ for $\theta = 20^\circ$, $N = 62500$, and $\Gamma = 2.13$. (a) At different times $t$ during one simulation, $t = 24.5$ ms corresponding to one period of vibration. Values of mean velocities in time and space are equal to zero. (b) Superposition of the waves. The solid lines represent fits to exponential envelopes (Eq. 12), here $v_y/\sqrt{gd} = \pm 0.115 \exp(-0.112 z/d)$.

Table 1: Expressions of the coefficients of the contact force model used in the DEM simulations. Here, $E$ is the Young modulus, $\nu$ the Poisson ratio, $e$ the restitution coefficient, and $\beta = \frac{\ln(e)}{\sqrt{\ln^2(e)+\pi^2}}$ the damping ratio.

| Coefficient | Particle/particle expression | Particle/wall expression |
|---|---|---|
| $k_n^* = k_n/\sqrt{\delta_n}$ | $\frac{E}{3(1-\nu^2)}\sqrt{d}$ | $\frac{2E}{3(1-\nu^2)}\sqrt{d/2}$ |
| $k_t^* = k_t/\sqrt{\delta_n}$ | $\frac{3(1-\nu)}{2-\nu}k_n^*$ | $\frac{3(1-\nu)}{2-\nu}k_n^*$ |
| $\gamma_n/\delta_n^{1/4}$ | $-\sqrt{\frac{5}{2}}\beta\sqrt{mk_n^*}$ | $-\sqrt{5}\beta\sqrt{\sqrt{2}mk_n^*}$ |
| $\gamma_t/\delta_t^{1/4}$ | $-\sqrt{\frac{5}{3}}\beta\sqrt{mk_t^*}$ | $-\sqrt{\frac{10}{3}}\beta\sqrt{\sqrt{2}mk_t^*}$ |

Table 2: Summary of the performed simulations with the properties that have been used: the relative roughness $d/\lambda$, the inclination angle $\theta$, the system size $N$ and the relative acceleration $\Gamma$.

| Gravity-driven regime $\theta > \theta_c$ | | | | Vibration-driven regime $\theta < \theta_c$ | | | |
|---|---|---|---|---|---|---|---|
| $d/\lambda$ | $\theta$ (°) | $N$ | $\Gamma$ | $d/\lambda$ | $\theta$ (°) | $N$ | $\Gamma$ |
| 1/3 | 21 | 112500-125000 | 0-0.021 | 1/3 | 20 | 37500 | 2.13 |
| | | 137500-150000 | 0.21 | | | | 4.26 |
| | 22 | 37500-50000 | 0-0.021-0.043 | | | | 6.40 |
| | | 75000-112500 | 0.13-0.21 | | | 62500 | 2.13 |
| | 24 | 12500-25000-37500 | 0-0.021-0.043 | | | | 4.26 |
| | | 62500-75000-112500 | 0.13-0.21 | | | | 6.40 |
| | 28 | 5000-12500-37500 | 0-0.021-0.043 | | | 112500 | 2.13 |
| | | 62500-87500-112500 | 0.13-0.21 | | | | 4.26 |
| 1/5 | 22 | 87500 | 0-0.13 | | | | 6.40 |

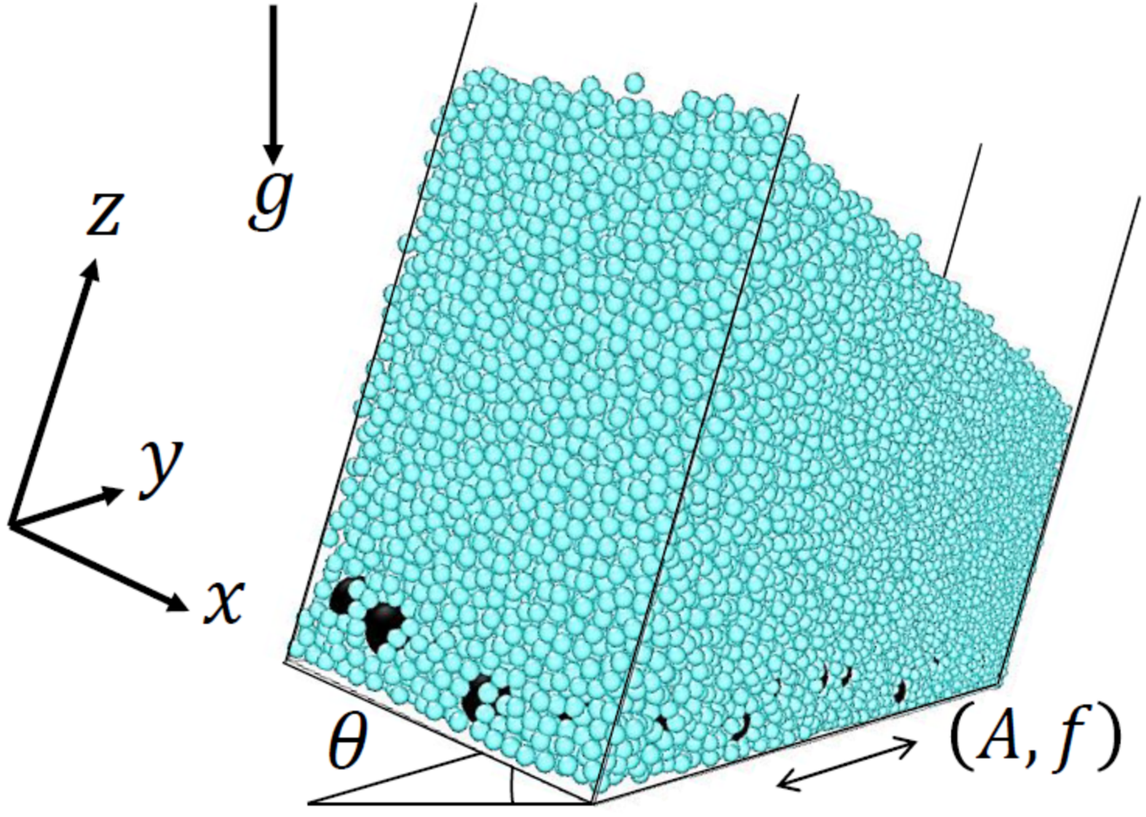
z
g
y
x
θ
(A, f)

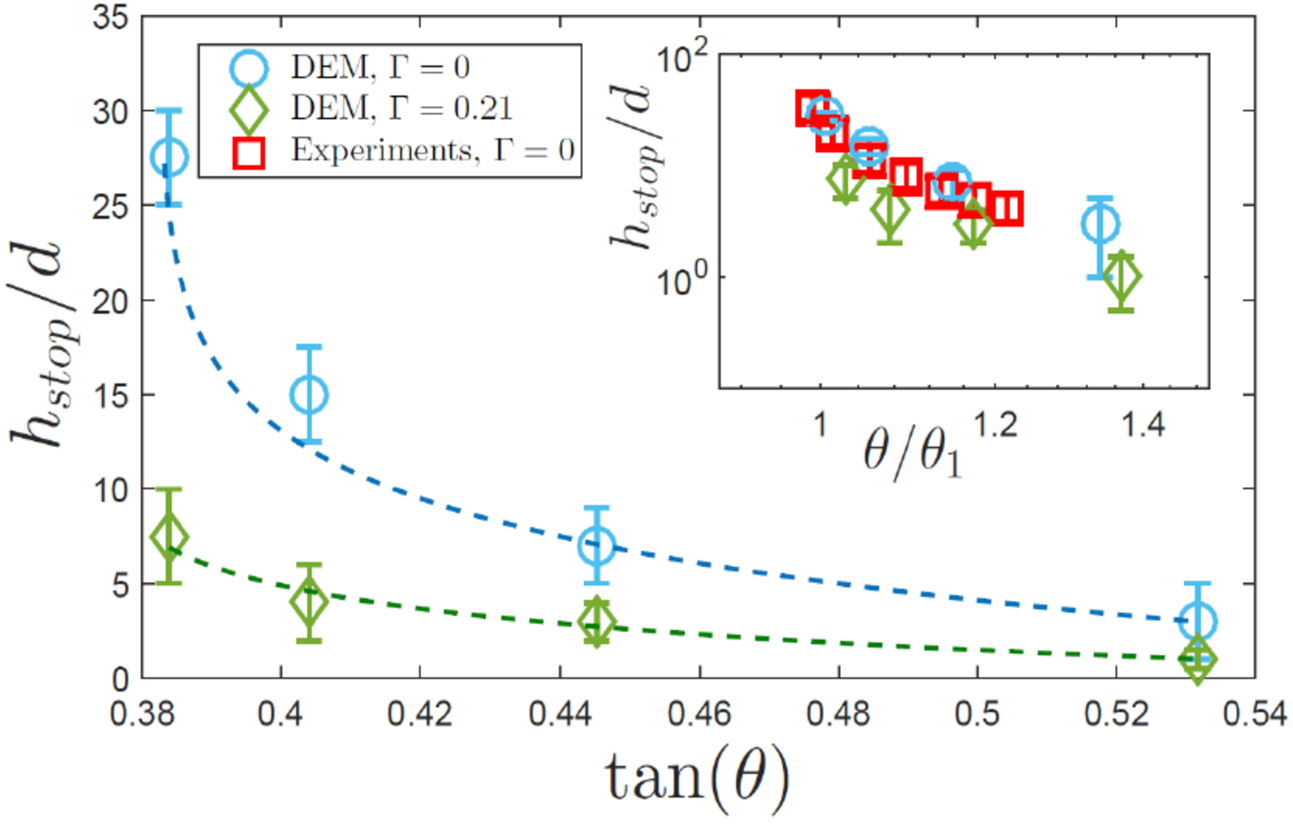
DEM, Γ = 0
DEM, Γ = 0.21
Experiments, Γ = 0
h_stop/d
tan(θ)
θ/θ_1
35
30
25
20
15
10
5
0
0.38
0.4
0.42
0.44
0.46
0.48
0.5
0.52
0.54
10^2
10^0
1
1.2
1.4